Construction and Building Materials 263 (2020) 120985

Contents lists available at ScienceDirect

Construction and Building Materials

journal homepage: www.elsevier.com/locate/conbuildmat

Internal curing of alkali-activated slag-fly ash paste with superabsorbent polymers

Zhenming Li [a], Shizhe Zhang [a], Xuhui Liang [a], José Granja [b], Miguel Azenha [b], Guang Ye [a,c,*]

[a] Microlab, Department of Materials, Mechanics, Management & Design, Faculty of Civil Engineering and Geoscience, Delft University of Technology, Delft, the Netherlands
[b] ISISE, Department of Civil Engineering, School of Engineering, University of Minho, Guimarães, Portugal
[c] Magnel Laboratory for Concrete Research, Department of Structural Engineering, Ghent University, Ghent, Belgium

HIGHLIGHTS

- Internal curing is applied to mitigate the autogenous shrinkage of alkali-activated slag and fly ash.
- The reaction rate and microstructures of the paste are comprehensibly investigated.
- The cracking potential and mechanical properties of the pastes are also studied.
- Internal curing by SAPs are proven a promising admixture for alkali-activated slag and fly ash.

ARTICLE INFO

Article history:
Received 20 May 2020
Received in revised form 7 September 2020
Accepted 14 September 2020
Available online 30 September 2020

Keywords:
Alkali-activated slag/fly ash
Autogenous shrinkage
Internal curing
Microstructure
Cracking
Mechanical properties

ABSTRACT

This study investigates the influences of internal curing on reducing the autogenous shrinkage of alkali-activated slag/fly ash (AASF) paste. The influences of internal curing with superabsorbent polymers (SAPs) on the reactions and microstructure of AASF paste are investigated. It is found that the SAPs absorb liquid mainly before the initial setting time of the paste. Afterwards, the liquid is gradually released, keeping the internal relative humidity of the paste close to 100%. The internal curing with SAPs can significantly mitigate the autogenous shrinkage of AASF paste, especially after the acceleration period of the reaction. The mitigating effect of internal curing is due to the mitigated self-desiccation in the paste, rather than the formation of a denser microstructure or expansive crystals. The cracking potential of AASF under restrained condition is also greatly mitigated by internal curing. Despite the slight reductions in the elastic modulus and the compressive strength, great improvement is obverted in the flexural strength of the paste. This work confirms the effectiveness of internal curing of AASF with SAPs and further provides a promising way to reduce the autogenous shrinkage of AASF without compromising its mechanical properties.

1. Introduction

The current construction sector contributes to one major part of global CO_2 emission, which predominantly relates to the production of cement. As reported in [1,2], ordinary Portland cement (OPC) production contributes to 5–8% CO_2 emission worldwide. According to the data from United States Geological Survey, a substantially increasing amount of cement is being produced in recent years [3]. The huge amount of cement production worldwide indicates a great future demand of binder materials, however, this demand conflicts with the request to reduce the emission of greenhouse gases [4].

To resolve this conflict, increasing research attention has been attracted to the exploitation of "greener" alternative binders which can partly or completely replace OPC in construction applications [5]. Among all alternative binders, alkali-activated materials (AAMs) have emerged as important candidates [6]. AAMs are defined as materials synthesized by an aluminosilicate precursor and an alkaline activator [7]. While OPC production requires the calcination of limestone which emits CO_2 and consumes energy [8–10], AAMs can be made from the industrial by-products, to which little environmental footprint is usually attributed [4,11]. The activators like sodium hydroxide and sodium silicate need to be produced from the manufacturing process, which does bring associated energy consumption and CO_2 emission [12]. However, because the activator usually accounts for<10% by mass of the

* Corresponding author.
E-mail address: G.Ye@tudelft.nl (G. Ye).

https://doi.org/10.1016/j.conbuildmat.2020.120985
0950-0618/

binder, the CO_2 emission per ton of binder is still much lower than that associated with OPC according to [7].

The two most widely utilized by-products as precursors for AAMs are ground granulated blast-furnace slag (hereinafter-termed slag) from the steelmaking and fly ash from the coal-fired electricity plants. The concrete using alkali-activated slag/fly ash (AASF) as binder material could be cement-free. It has been found that AASF materials can show good mechanical properties and durability, however, they can also show large autogenous shrinkage [11–26]. Autogenous shrinkage is defined as *the bulk shrinkage of a closed, isothermal, binder material not subjected to external forces* [13]. Unlike drying shrinkage and plastic shrinkage that can be eliminated by protecting the material from drying [14], autogenous shrinkage is a self-induced shrinkage driven by internal forces and can develop fast at the early age when the strength of the material is low. The autogenous shrinkage may induce cracking of the materials under restraint conditions, which could lead to a series of problems with regard to aesthetics, strength, and durability. As reported in the literature [15–17], AASF materials generally show larger autogenous shrinkage than the commonly used OPC-based systems, particularly when the slag content is high. The large autogenous shrinkage has been considered a conundrum that impedes the applications of AASF as a binder in construction materials [15,17,18].

Many studies have been conducted to explore shrinkage-mitigating strategies for slag and fly ash-based AAMs, such as using expansive agent, shrinkage-reducing agent (SRA), or elavated temperature.

The results of Li et al. [19] showed that the expansion induced by MgO can compensate the shrinkage of AASF and meanwhile the early age strength was improved. Their results were confirmed by Yang et al. [20] who found that the addition of reactive MgO can mitigate both the autogenous shrinkage and the drying shrinkage of AASF.

Hu et al. [21] reported a greatly mitigated autogenous shrinkage of alkali-activated slag (AAS) by an SRA based oxyalkylene alcohol. The mechanism was attributed to the decrease in the capillary tension. Polypropylene glycol was found to have similar shrinkage-mitigating effects without decreasing the strength [22,23]. However, some SRA show side effects (e.g. strength loss) when applied in AAMs [24–26]. For example, Bílek et al. [27] studied the effects of hexylene glycol-based SRA on the shrinkage of AAS mortar and found an inevitable decrease in compressive strength. Collins and Sanjanyan [28] applied a SRA into AAS concrete to reduce the magnitude of drying shrinkage, but the cracking time of the concrete was not delayed due to the simultaneously decreased tensile strength.

Li et al. [29] found that the incorporation of metakaolin into AAS system can mitigate the early age autogenous shrinkage of the paste. The mechanism mainly lies in the enlarged porosity and reduced chemical shrinkage of the paste due to the presence of metakaolin. The drop of internal relative humidity (RH) in the paste is therefore mitigated.

Bakharev et al. [30] and Ye [31] reported that elevated temperature curing can mitigate the drying shrinkage of AAS. The mechanism lies in the decrease in visco-elastic/visco-plastic compliance of C-(N)-A-S-H gels in elevated temperatures. This indicates that this strategy may also mitigate the autogenous shrinkage. According to a previous study [32], a large part of the autogenous shrinkage of AAS belongs to visco-elastic deformation. However, elevated-temperature curing may be unsuitable for cast-in-situ concrete due to the strict requirements of curing conditions. Besides, the elevated temperature curing would accelerate the reaction process [33] and cause a rapid setting of AAS and AASF.

Internal curing is a promising way to mitigate the self-desiccation of a paste without need to retard the reactions, because the internal curing agents can directly supply liquid to the matrix to compensate for the self-desiccation [34]. The two most widely used types of liquid reservoirs to provide internal curing are light-weight aggregates and superabsorbent polymers (SAPs). As reported by Jensen [35], SAPs normally have a cross-linked structure, which can absorb water many times of its own weight. The water stored in SAPs will be released to the surroundings during the hardening of the paste. Compared with light-weight aggregates, SAPs can induce less strength loss of the matrix and are of lower cost, therefore they are widely used as an internal curing agent [36,37].

Internal curing by SAPs has been widely recognized effective in OPC-based systems [35,38–42], while for AAMs, only limited experimental studies concerning internal curing have been conducted [43–45]. Oh and Choi [44] reported that SAPs can reduce the autogenous shrinkage of AAS mortar. In AAS paste, internal curing by SAP is also effective according to Li et al. [46]. On AASF systems, which probably have better application prospects than AAS systems due to the postponed setting and the lower shrinkage [7], fewer studies can be found with the utilization of internal curing. Tu et al. [43] observed a reduced autogenous shrinkage of AASF paste when SAPs were incorporated. However, since no reference mixture (with increased liquid content but without SAPs) was set in [43], it was unable to distinguish whether the reduced shrinkage of the paste with SAPs were due to the internal curing or due to the increased liquid content. The shrinkage-mitigating mechanism of SAPs in AASF is still poorly understood. Furthermore, the influences of internal curing on the microstructure evolution and reaction rate of AASF need also better understandings.

Therefore, this study aims to investigate the performance of SAPs as internal curing agents in view of reducing the autogenous shrinkage of AASF pastes and clarify the mechanisms behind. The SAPs dossage in AASF was determined based on the absorption capacity of SAPs in alkali solutions. The reaction products, reaction kinetics and microstructure of the internally cured paste are characterized and compared with those of the control mixture. The mechanical properties, such as strength and elastic modulus of the pastes are also investigated. The mitigating effects of internal curing on the autogenous shrinkage and the self-induced stress are then examined and discussed.

2. Materials, mixtures and methods

2.1. Raw materials

The primary raw materials were slag and Class F fly ash (EN 450, ASTM C618). The chemical compositions of them are shown in Table 1. Slag and fly ash show a d_{50} of 18.3 μm and 48.1 μm, respectively.

The alkaline activator was prepared by dissolving sodium hydroxide pellets and commercial sodium silicate solution. For 1000 g of precursor, an activator containing 384 g of water, 1.146 mol of SiO_2 and 0.76 mol of Na_2O was applied. The activator was allowed to cool down to room temperature before casting.

Solution-polymerized SAPs in dry state were used. The backscattered scanning electron (BSE) image of SAPs particles is illustrated in Fig. 1. The SAPs are in irregular shape and in size of up to 200 μm. The SAPs were homogenously mixed with the precursors before the adding of activator.

2.2. Mixture design

The l/b ratio of plain AASF paste as control mixture is 0.5. With internal curing, the liquid provided by SAPs should compensate for the volume of chemical shrinkage of the paste [47]. In this study,

Table 1
Chemical compositions of the raw materials determined by X-ray fluorescence.

Oxide (%)	CaO	Al_2O_3	SiO_2	MgO	Fe_2O_3	SO_3	K_2O	TiO_2	Other	LOI
Slag	40.5	13.3	31.8	9.3	0.5	1.5	0.3	1.0	0.2	1.3
Fly ash	4.8	23.8	56.8	1.5	7.2	0.3	1.6	1.2	1.6	1.2

LOI = Loss on ignition.

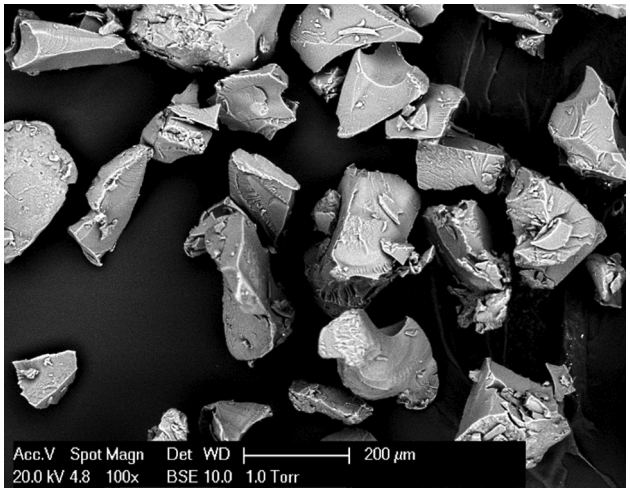

Fig. 1. BSE image of SAPs particles in dry state.

the ultimate chemical shrinkage of AASF paste was determined by taking the chemical shrinkage measured by dilatometry till the age of 28 days [48,49], which is 0.026 ml/g. Taking also into account the density of the activator, 1.23 g/cm^3, the extra liquid provided by the SAPs should be 0.032 g per gram of binder. According to the absorption capacity of the dry SAPs in the alkaline activator ($NaOH/Na_2SiO_3$ solution), 20 g per gram of SAP, as obtained in a previous study [46] using the teabag method, the desired amount of SAPs is calculated to be 0.16% by mass of the binder (the calculating equations can be found in [46]).

The compositions of three mixtures, i.e., the control mixture, the mixture with extra liquid without SAPs and the mixture with extra liquid and SAPs are shown in Table 2. The basic l/b means the liquid not absorbed by the SAP.

2.3. Experimental methods

2.3.1. Reaction products

The pastes cured for 1 day and 7 days were ground into powders and the reaction was stopped by solvent exchange method recommended by Scrivener et al. [50].

The chemical bonds formed within the reaction products were determined by Fourier transform infrared spectroscopy (FTIR) using a Spectrum TM 100 Optical ATR-FTIR spectrometer over the wavelength range of 600 to 4000 cm^{-1}. The resolution of the measurement is 4 cm^{-1}.

X-ray diffraction (XRD) was performed to detect the possible crystals formed in the paste. A Philips PW 1830 powder X-ray diffractometer, with Cu Kα (1.5406 Å) radiation, tube setting of 40 kV and 40 mA, a step size of 0.030° and a 2θ range of 5–70°, was used to perform the test.

2.3.2. Reaction heat and setting time

The reaction heat flow of the pastes was measured by isothermal calorimetry using a TAM Air conduction calorimeter. The temperature during the experiment was controlled to be 20 ± 0.02 °C. Since the low flowability of the pastes led to the need for a high energy mixing process, the AASF pastes were prepared externally. 5 g of freshly mixed paste was carefully transferred into a small glass bottle. Immediately afterwards, the bottles were closed and put into individual channels. The preparation took around 15 min. The data was recorded every 1 min until 7 days. Both the heat flow and cumulative heat were normalized by the mass of the binder.

The initial and final setting times were measured according to NEN-EN 196–3:2005. An automatically recording Vicat apparatus (Controls VICATMATIC 2) was used. The measurement intervals were set to be 10 min before initial setting and 1 min afterwards [51].

2.3.3. Microstructure evolution

To detect the big voids originated from the incorporation of SAPs and monitor the movement of liquid from SAPs, X-ray computed tomography (CT) scan was utilized. The mixture AASF0.532-SAP was scanned using a Phoenix Nanotom Nano-CT-Scanner. The cast sample was sealed after casting and scanned at four different ages, including 1 h, 8 h, 1 day and 7 days. For each scan, 2030 images from the top view were obtained. The spatial resolution under these configurations was 5 μm. Through using the Phoenix Datos|x software, the reconstruction work was conducted.

The fractured surface of internally cured pastes AASF0.532SAP and the voids left by desorption of SAPs were observed using scanning electron microscope (SEM) by a Philips- XL30-ESEM in secondary electron mode under high vacuum condition.

Nitrogen absorption is able to detect small pores (from 0.2 to 200 nm) in the paste. The pastes cured for 7 days were crushed into small pieces (2–4 mm) and the reaction was stopped by solvent exchange method [50]. Nitrogen adsorption test was performed to measure the pore structure (from 0.3 to 300 nm) of the pastes by using Gemini VII 2390V1.03 (micromeritics, Brussel, Belgium). The relative pressure ranges from 0.05 to 0.99. The isotherms is obtained based on Barrett-Joyner-Halenda models (BJH) [52].

2.3.4. Internal RH and autogenous shrinkage

Measurements of internal RH in AASF paste were performed by Rotronic hygroscopic DT stations [53]. The dimension of the sample container is 30 mm. The paste was crushed into small pieces

Table 2
Mixture design of AASF paste with and without SAP.

Mixture	Slag	Fly ash	Total l/b	Basic l/b	Entrained l/b	SAPs
AASF0.5	0.5	0.5	0.5	0.5	0	–
AASF0.532	0.5	0.5	0.532		0	–
AASF0.532SAP	0.5	0.5	0.532		0.032	0.0016

around 0.5 cm^3 and immediately inserted into the hermetic measuring chambers. The distance between sample and humidity sensor was <30 mm. For the measurement of the RH of the pore solution, the same sensors are used. The pore solution was extracted by hydraulic piston from the corresponding paste and was collected into small plastic vessels. The vessels were then sealed to minimize the carbonation of the solution until put into the hermetic chambers for measurement.

Two measurements for each sample were conducted simultaneouly at two different HC2-AW measuring cells. The nominal accuracy of the sensors was reported to be within ± 1% RH [54]. Calibration of the sensors were conducted regularly using three standard salt solutions with equilibrium RH at 65%, 80% and 95%.

The RH due to menisci can be approximated according to Eq. (1) [55].

$$RH = RH_S \cdot RH_K \quad (1)$$

where RH is the internal RH of the paste, RH_S is the RH caused by the ions in the pore solution and RH_K is the RH caused by the curvature at the gas–liquid interfaces.

Corrugated tubes with a length of 425 mm and a diameter of 28.5 mm were utilized to measure the linear autogenous shrinkage of AAS pastes according to ASTM C1968 [56]. Three replicates were measured for each mixture. The length changes were automatically measured by linear variable differential transformers (LVDTs) until 7 days. After that, the evolution of the autogenous shrinkage becomes slow so the test is stopped. The automatic measurements show a low scatter for triplicate samples, with the relative standard error in the range of 1–2%.

2.3.5. Autogenous shrinkage-induced stress and cracking

Ring test was utilized to monitor the stress evolution in AASF pastes resulting from the restrained autogenous shrinkage [57,58]. The geometry of the rings is shown in Fig. 2. Strain gauges were attached to the inter surface of the inner ring. The top surface of the ring was sealed by aluminium-asphalte tape and the bottom edge of the ring was sealed by Vaseline to minimize the moisture loss. The maximum stress (σ_{max}) in the paste was estimated by the strain of the steel (ε_{steel}), as shown by Eq. (2) [59].

$$\sigma_{max} = -\varepsilon_{steel} \cdot E \cdot \left(\frac{R_{OI}^2 - R_{II}^2}{2R_{OI}^2}\right)\left(\frac{R_{OP}^2 + R_{OI}^2}{R_{OP}^2 - R_{OI}^2}\right) \quad (2)$$

where E is the elastic modulus of the steel. The inner radius (R_{II}) and outer radius (R_{OI}) of the inner ring are 75 mm and 87.5 mm, respectively. The outer radius of the paste ring (R_{OP}) is 125 mm.

2.3.6. Mechanical properties

The flexural and compressive strength of AASF paste were tested in accordance with NEN-196-1 [60]. The prismatic samples for flexural strength test have a size of 40 × 40 × 160 mm^3. The halves of the broken prisms are then used for compressive strength test. The elastic modulus of the paste was measured using Elasticity Modulus Monitoring through Ambient Response Method (EMM-ARM [61]) from casting until 7 days. The EMM-ARM method applied herein is based on the continuous monitoring of the first resonant frequency of a 450 mm span composite cantilevered beam with circular cross-section (outer shell with a 20 mm thick acrylic tube, and inner 16 mm corresponding to the material under testing). Based on the knowledge of all geometric and mass features of the testing system, it is possible to infer the elastic modulus of the tested material through application of the dynamic equation of motion of the beam. The detailed procedure was described in [61]. Three replicates were tested for each mixture.

3. Results and discussion

3.1. Reaction products characterization

According to [24], some admixtures can be chemically unstable in media with a high pH, thus they might have some influences on the reactions. To investigate the possible influence of internal curing with SAPs on the reaction products of AASF, paste specimens with and without SAP were characterized by FTIR and XRD.

As shown in Fig. 3(a), the broad humps, also known as the main bands, of the FTIR spectra of the three pastes cured for 1 day locate at the same position, 950 cm^{-1}, which represents the vibration of Si–O bonds in Q^2 units [62]. This signal is representative of C-(N)-A-S-H type gel [62]. The spectra also show a small bands at 815 cm^{-1}, which is attributed to the symmetric stretching vibrations of Si–O (Q^1) [63]. The similar bands in the spectra for pastes indicate that the three mixtures have similar reaction products, C-(N)-A-S-H type gel, at 1 day. The small peak at 855 cm^{-1} in the spectra is due to the unreacted slag. Only minor difference among the spectra for the three pastes cured for 1 day is observed, which is the small peak shoulder at 874 cm^{-1} found in the spectra for AASF0.532 and AASF0.532SAP while not in that for AASF0.5. This signal is attributed to the bending vibration of CO_3^{2-}, indicating that carbonation occurred in AASF0.532 and AASF0.532SAP during sample preparation which is unexpected [64]. This can be confirmed by the more obvious bands in the range from 1350 to 1550 cm^{-1} in the spectra for AASF0.532 and AASF0.532SAP [65]. Except for the bands due to carbonation, no obvious difference can be observed in the spectra for pastes cured for 1 day.

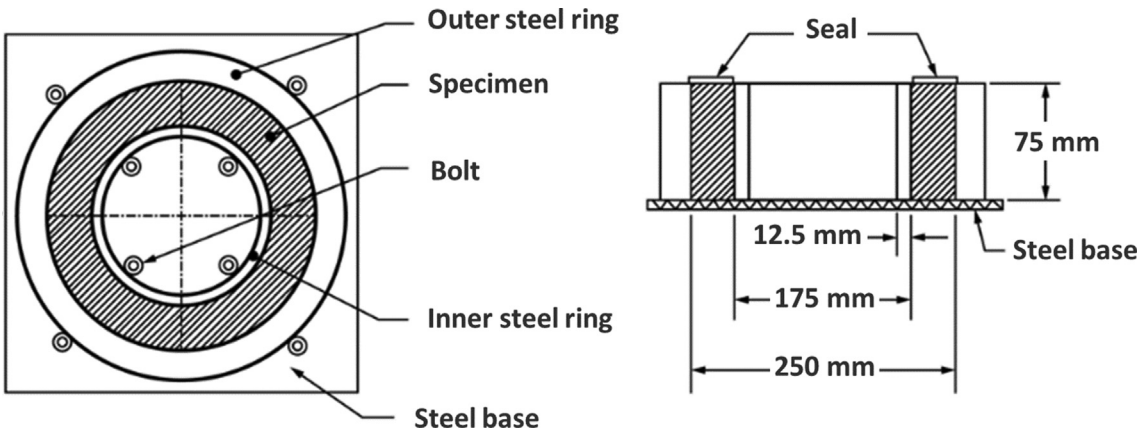

Fig. 2. Dimensions of the steel rings.

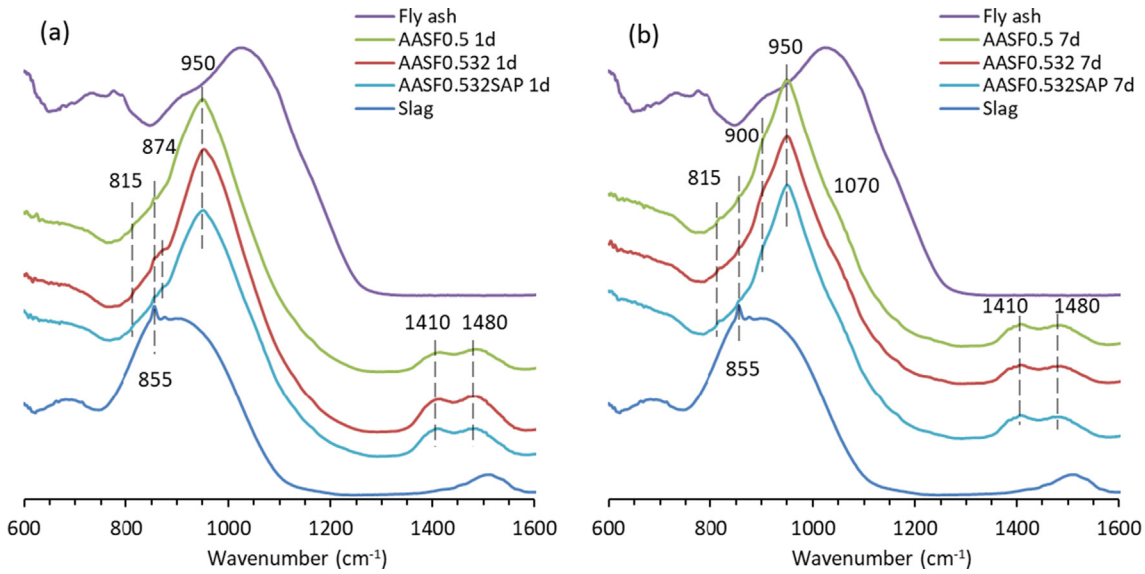

Fig. 3. FITR spectra of AASF pastes at the ages of 1 day (a) and 7 days (b), in comparison with precursors (slag and fly ash).

At the age of 7 days, the main bands of the spectra become sharper as shown in Fig. 3(b), indicating the formation of more reaction products. Besides, shoulders at around 900 cm^{-1} and 1070 cm^{-1} also become distinct in the spectra for pastes. These signals are attributed to the deformational and asymmetrical stretching vibrations of Si-O-Al or Si-O-Si [26,63,66], respectively, as evidences of more reaction products being formed in the paste with longer curing time. It should be noted that at 7 days, the three pastes show almost identical FTIR spectra. The information presented in Fig. 3 (a) and (b) indicates that the internal curing has little effect on the reaction products of the paste during the first week of curing.

The XRD results of the precursors and the pastes are presented in Fig. 4. The curves for AASF pastes all show a broad hump at 29° and a small band at around 50° on both 1 day and 7 days. This confirms that similar amorphous reaction products are formed in the pastes with and without SAPs. From 1 day to 7 days, the intensity of the main band of the curves increases with reference to the peaks for inert crystals like quartz. This indicates that more reaction products are formed with age. This is consistent with the results shown in Fig. 3. Besides the crystals (mainly mullite, quartz and hematite) originated from the unreacted fly ash, no crystals are newly formed during the first week of reaction. This information is important in analysing the pore structure of AASF paste and the autogenous shrinkage results in latter sections.

3.2. Reaction rate and setting

The heat flow and the cumulative heat of AASF pastes with and without SAPs are presented in Fig. 5. A dormant period of around 11 h is followed by a main peak corresponding to an acceleration period. The main heat flow peak is amplified in Fig. 5(a).

As shown in Fig. 5(a), the main heat flow peak of AASF0.532 appears later and has a slightly higher intensity than that of AASF0.5. With higher l/b ratio, the absolute amount of silicate species and alkali ions available are also higher in the interstitial space together with the increased amount of water. Therefore, a longer time is needed for the dissolution of the precursors to provide more Ca^{2+} and Al^{3+}. Only after critical Al/Si and Ca/Si are reached, the the C-(N)-A-S-H gels can rapidly form. As a result, the main peak appears later for AASF0.532. Nonetheless, the intensity of the main peak of AASF0.532 is higher than AASF0.5. due to the exsitence of larger amonts of ions, viz. reactants. This is inline with the experimental observations as shown in Fig. 5(a). The larger amount of reactants from the activator results in a higher total heat release of AASF0.532 as could be seen in Fig. 5(b).

When SAPs are present, the main heat release peak is also delayed but its intensity is lower than that of the control mixture. Unlike in AASF0.532, the extra activator in AASF0.532SAP is stored in the SAPs particles after casting and is therefore not directly available for the reactions [67]. During the reaction, the gradual releasing of the activator from SAPs can dilute the Ca^{2+} and Al^{3+} in the present pore solution and delay the process of reaching critical concentrations of these ions. This explains why the peaking time of the reaction rate is slightly delayed and the intensity of the main peak is lowered when SAP is present. At the age of 7 days, there is still a bit activator stored in SAPs which has not participated in the reactions in the interstitial space yet (this will be verified in section 3.4). Therefore, the cumulative heat of AASF0.532SAP is slightly lower than that of AASF0.532.

The initial and final setting times determined by Vicat method are shown in Table 3. Increasing the l/b ratio of the paste without SAPs leads to increases in both initial setting time and final setting time. With the incorporation of SAPs, the paste shows similar setting times to the control mixture. This is probably because these two mixtures have similar basic l/b ratio, which dominates the setting process.

3.3. Microstructure evolution

The big voids originated by SAPs is observed by CT scan and SEM. Fig. 6(a)–(d) show the evolution of a representative cross-section of AASF0.532SAP obtained by X-ray CT scan at different curing ages. At 1 h, SAPs particles with liquid stored inside can be observed embedding in the paste, as shown in Fig. 6(a). With the increase of time, the size of the SAPs particles does not increase, indicating that the absorption of liquid occurs mainly within the first hour after mixing, which corresponds to the initial setting time of the paste. At 8 h, desorption of liquid already began, indicated by the grey scale change of the middle part of the SAPs from light grey to black (marked by the arrows in Fig. 6(b)). The area of voids in SAPs increases with time, indicating the gradual desorption of the SAPs. At 7 days, a big part of the liquid in SAPs has been consumed.

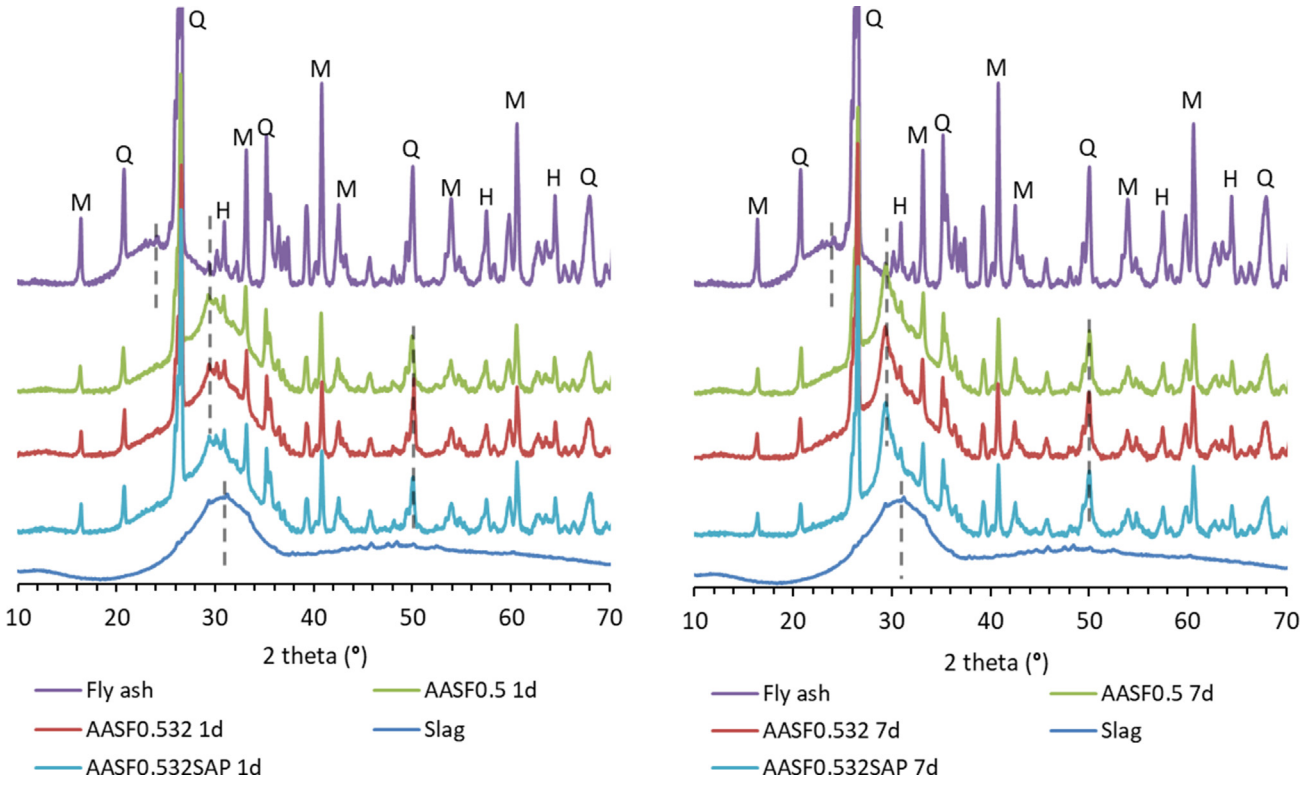

Fig. 4. XRD of AASF paste at the ages of 1 day (a) and 7 days (b), in comparison with precursors (slag and fly ash). M, Q and H stand for mullite, quartz and hematite, respectively.

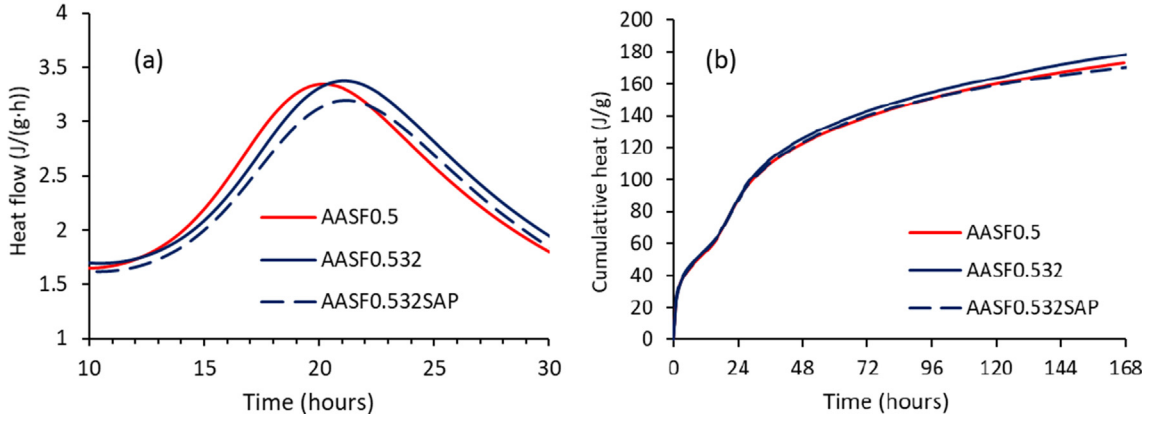

Fig. 5. Heat flow (a) and cumulative heat (b) of AASF pastes.

Table 3
Setting times of AASF pastes.

Mixture	Initial setting time (min)	Final setting time (min)
AASF0.5	63	103
AASF0.532	68	133
AASF0.532SAP	64	109

Additionally, the voids originated from SAPs remain unfilled during the first week of curing. This may be due to the dense microstructure so that it is hard for the ions to diffuse into the space occupied by SAP to form reaction products. The lack of reaction products formed in the SAP-induced voids indicates that the incorporation of SAPs in AASF paste does not effectively facilitate the formation of more reaction products through providing extra space. This confirms the similar reaction degrees of AASF paste with and without SAP as shown in Fig. 5. Due to the presence of liquid in the SAPs, the self-desiccation during the first week would be mitigated or eliminated. This will be verified in section 3.4.

Fig. 7 shows one representative image obtained by SEM on the fracture surfaces of AASF0.532SAP paste cured for 7 days. From the images, the dry SAPs and the surrounding AASF paste can be clearly distinguished based on their surface features: the SAP particle has a locally porous microstructure while the AASF paste is dense and homogenous. Unreacted fly ash particles can be observed embedded on the fractured surface. The SAP particle shown in Fig. 7 has a big void inside, with a smooth curved surface, which is in line with the inside-out drying process observed by CT scanning results in Fig. 6. No apparent reaction products can be observed in the voids left by SAP.

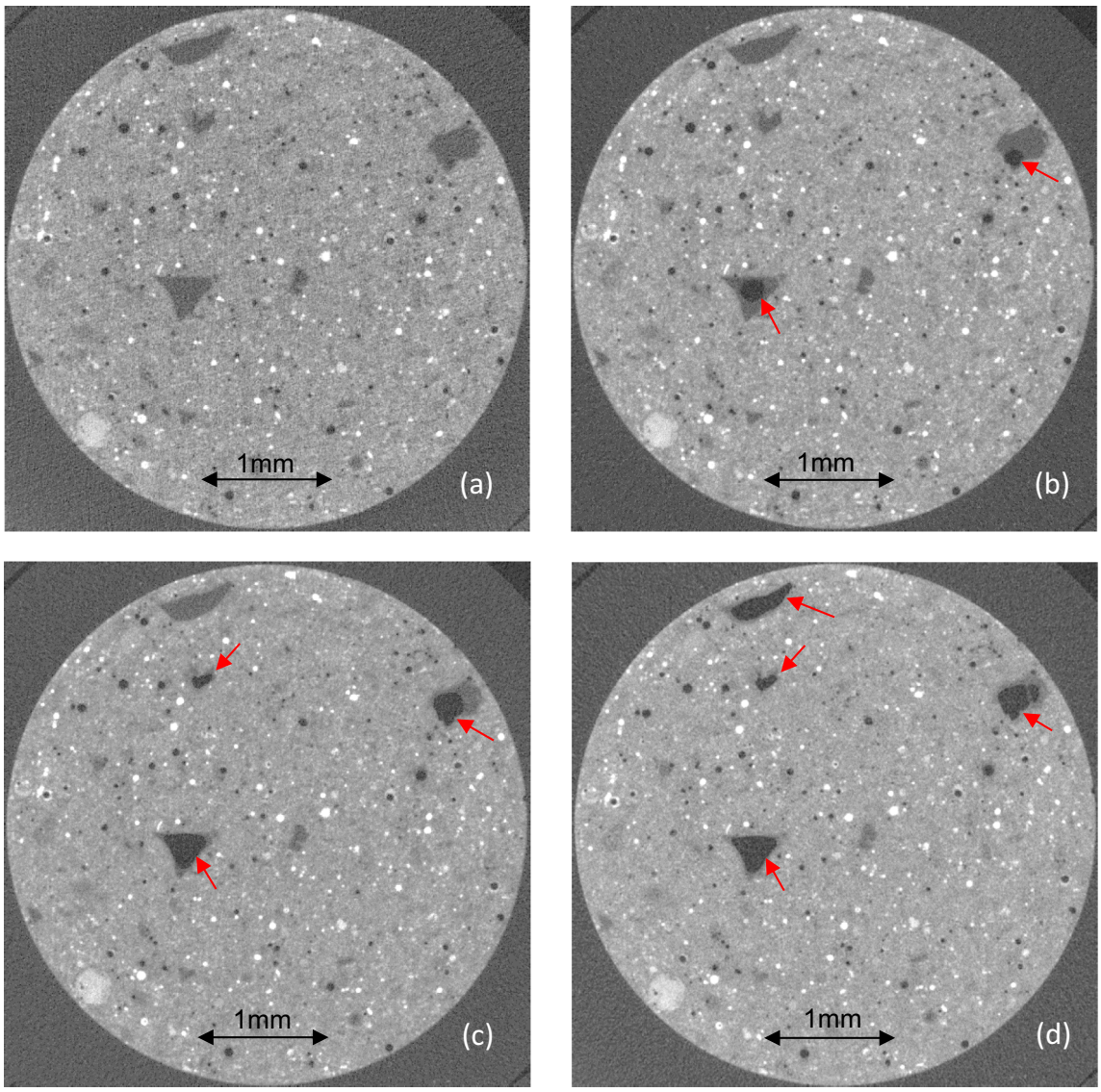

Fig. 6. A representative cross-section of AASF0.532SAP paste obtained by X-ray CT scan at (a) 1 h, (b) 8 h, (c) 1d and (d) 7d.

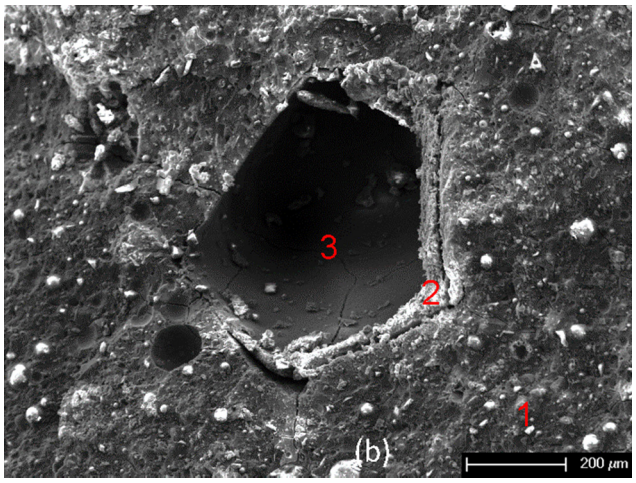

Fig. 7. SEM images of the SAP-originated voids in paste AASF0.532SAP cured for 7 days. The red coloured number 1 indicates the paste, 2 indicates the dry SAPs and 3 indicates the SAP-originated voids. (For interpretation of the references to colour in this figure legend, the reader is referred to the web version of this article.)

Nitrogen absorption was applied to further characterize the microscale pore structure of the pastes in the range of 2 nm–200 nm. As shown in Fig. 8, AASF0.5 and AASF0.532SAP show generally similar pore structure in the range detected by nitrogen absorption. AASF0.5 shows a critical pore size at around 5 nm while AASF0.532SAP shows a critical pore size at around 6 nm. The minor difference in the critical pore size may be due to the pores contained within the dry SAPs particles, which were also detected by the nitrogen. Both AASF0.5 and AASF0.532SAP show few capillary pores (>10 nm). The results in Figs. 6 to 8 indicate that internal curing with SAPs affect the pore structure of AASF paste mainly by introducing big voids originated from the SAPs rather than modifying the capillary and gel pore structures.

3.4. Internal RH and autogenous shrinkage

For AASF0.5 and AASF0.532SAP paste, the measured *RH*, measured RH_S of their pore solutions and the calculated RH_K (see Eq. (1)) are shown in Fig. 9. It can be seen that the RH_S of the pore solutions is lower than 100% due to the presence of ions. The RH_K of AASF0.5 decreases with time, indicating the occurrence of self-desiccation. When the internal curing is applied, the RH_K of the

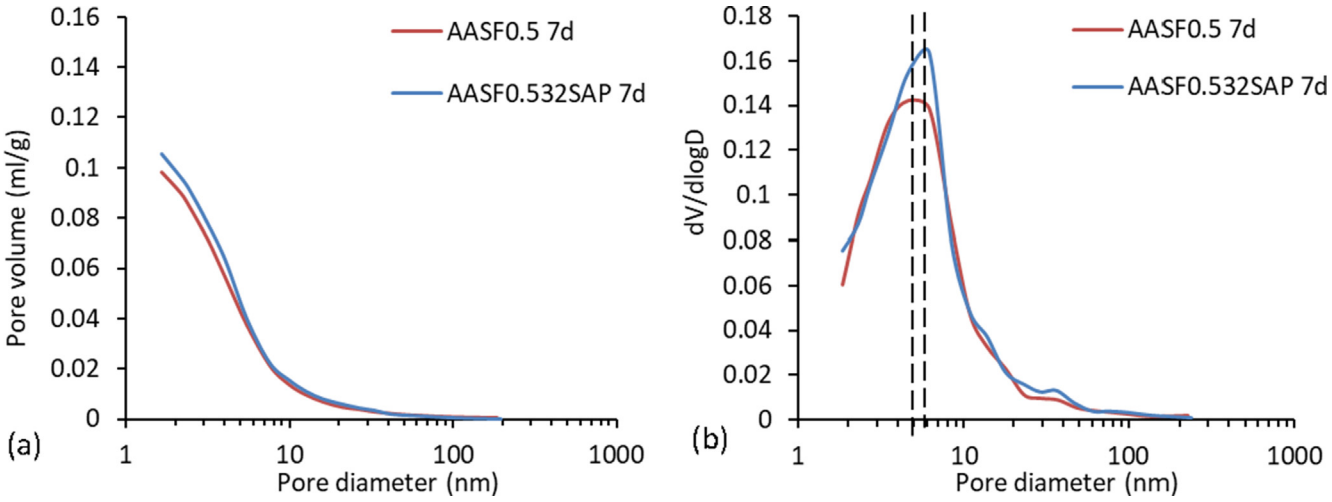

Fig. 8. Pore volume (a) and differential curves (b) for AASF0.5 and AASF0.532SAP at the age of 7 days.

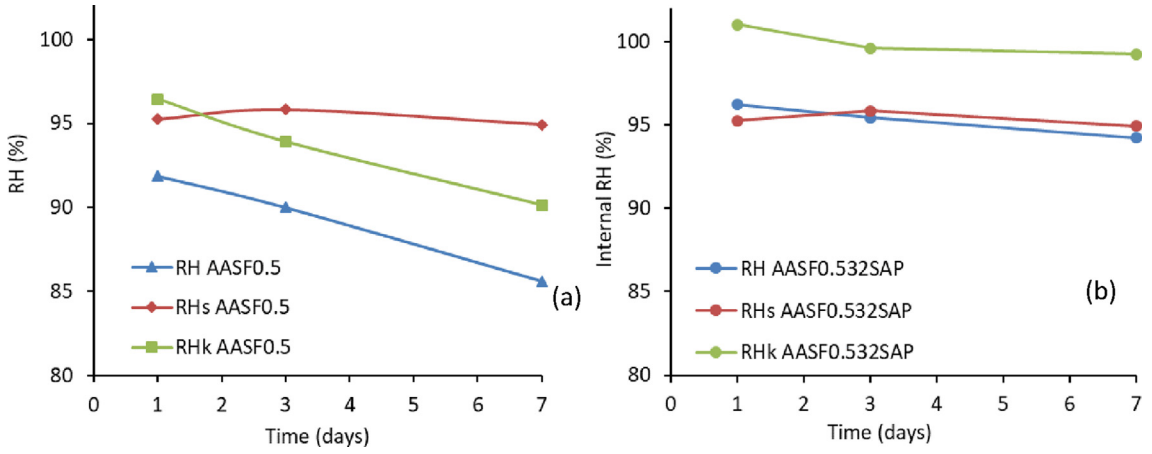

Fig. 9. Internal RH of AASF0.5 (a) and AASF0.532SAP (b).

paste remains around 100% in the period of study. This implies that the self-desiccation in AASF paste is successfully impeded by the internal curing with SAPs. The calculated RH_K of AASF0.532SAP in the first day is a bit higher than 100%. This is probably due to the experimental errors in measuring *RH* and RH_S.

The autogenous shrinkage of AASF pastes is shown in Fig. 10. The curves shown in Fig. 10(a) are zeroed at the final setting time of the paste. It can be seen that by only increasing the l/b without adding SAPs, the autogenous shrinkage is only reduced slightly. With the addition of SAP, the autogenous shrinkage can be effectively mitigated by more than 50% at 7 days. As shown in previous sections, AASF paste with internal curing has similar reaction products, reaction rate and pore structure to the control mixture. Therefore, it can be concluded that the autogenous shrinkage is effectively mitigated by internal curing due to the increased RH, rather than the formation of a denser microstructure with lower deformability or the formation of expansive crystals that can compensate the shrinkage.

It is also noteworthy that the mitigation effect of SAPs only becomes predominant after the acceleration period. In the first 20 h, which corresponds to the dormant and acceleration period (Fig. 5), AASF0.532SAP shows similar autogenous shrinkage to AASF0.5, although the RH of the paste is kept close to 100% (see Fig. 9). This indicates that the self-desiccation may not be the only mechanism to cause the autogenous shrinkage of AASF at the very early age [32]. The mechanism and mitigation strategy of autogenous shrinkage in the early stage needs further studies. Nonetheless, Fig. 10 clearly shows that the autogenous shrinkage of AASF after the first day can be substantially mitigated by internal curing, which is beneficial for engineering application of AASF.

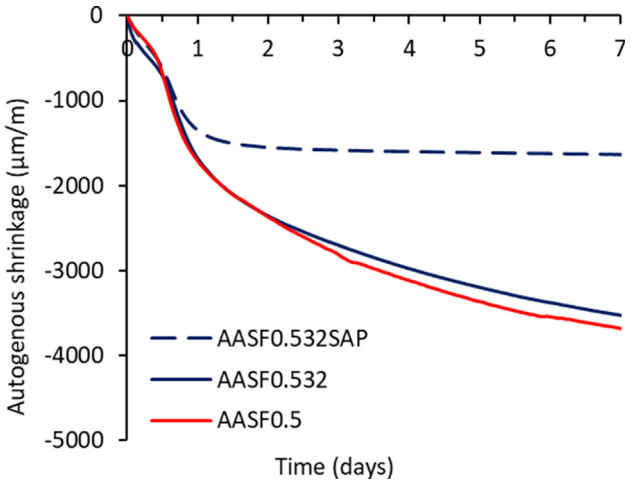

Fig. 10. Autogenous shrinkage of AASF pastes.

3.5. Autogenous shrinkage-induced stress and cracking

The autogenous shrinkage-induced stresses in AASF0.5, AASF0.532, and AAS0.532SAP measured with the ring test are compared in Fig. 11(a). For better illustration of the results at early age, the results within the first 60 h are shown in Fig. 11(b). The autogenous shrinkage-induced internal tensile stress gradually increases with time until the cracking of paste occurs, which is indicated by a sudden drop in the stress to around zero.

The control mixture AASF0.5 cracked at 2.2 days when the stress reached 2.7 MPa. On the other hand, increasing the l/b ratio to 0.532 delayed the cracking but only slightly. The failing stress of AASF0.532 was 1.71 MPa, which was lower than that of AASF0.5, indicating a lower tensile strength of the paste with increased l/b ratio. The stress rates at the cracking times of AASF0.5 and AASF0.532 are both higher than 0.34 MPa/day. According to ASTM C1581 [68], the cracking potential of both non-SAPs pastes is classified as "high" (Table 4).

With internal curing, the cracking did not occur until 29 days. The stress in AASF0.532SAP at cracking time is 6 MPa, indicating a high tensile strength of the in paste by internal curing. The stress rate at 29 days is 0.13 MPa/day, which more than 60% lower that of AASF0.5. According to Table 4, the cracking potential of AASF0.534-SAP is "moderate-low" or "low". These results indicate the internal curing can effectively mitigate the cracking potential of AASF paste, which cannot be realized by only increasing the l/b of the paste.

Another phenomenon can be noticed is that the stress in AASF0.532SAP experienced a second rapid increase starting at around 3 days. This increase is probably due to the inevitable drying of the sample in the ring, since the autogenous shrinkage of AASF0.532SAP already stabilized after the first day, as shown in Fig. 10. As presented in section 2.3.5, aluminium-asphalte tape and Vaseline were used to seal the ring, but moiture loss is still possible especially at long term. Since the weight of the whole ring test set-up was beyond the mearsuing range of the balance in the laboratory, the weight constancy of the sample was not checked. Further study is needed to find a better sealing measure (possibly by hot paraffin wax).

3.6. Mechanical properties

The compressive and flexural strength of AASF pastes is shown in Fig. 12. It can be seen that the compressive strength at both 1 day and 7 days slightly decreases with increasing l/b ratio, since higher l/b ratio normally means higher porosity of the paste especially at early age. At 28 days, the difference in the compressive strengths of AASF0.5 and AASF0.532 is smaller than the error range. With addition of SAPs, the compressive strength of AASF paste decreases considerably due to the macro-level voids induced by SAPs particles.

Table 4
Classification of cracking potential according to ASTM C1581 [68].

Average stress rate S (MPa/day)	Cracking time t_{cr} (days)	Potential for cracking
$S \geq 0.34$	$0 < t_{cr} \leq 7$	High
$0.17 \leq S < 0.34$	$7 < t_{cr} \leq 14$	Moderate-High
$0.10 \leq S < 0.17$	$14 < t_{cr} \leq 28$	Moderate-Low
$S < 0.10$	$t_{cr} > 28$	Low

The flexural strength of the paste also decreases with increasing l/b ratio in the ages studied for the samples without SAPs. This is consistent with the ring test results (see Fig. 11), which showed that AASF0.532 had a lower failure stress than AASF0.5. When SAPs are incorporated, a similar flexural strength to that of the control mixture is shown at 1 day. At 7 days, however, a considerably higher flexural strength is shown by internally cured paste than the other two mixtures. According to eurocode [69], the tensile strength of a paste is linearly related to the flexural strengh measured with 3-point bending. Hence, it can be concluded that AASF0.532 has higher tensile strength than the other mixtures at these ages. At 28 days, the differences become smaller. The higher tensile strength but lower internal stress in AASF0.532SAP determine a later cracking time of the paste, as in line with the results shown in Fig. 11.

The flexural strength of AASF0.5 and AASF0.532 decreases from 1 day to 7 days, which may be due to the development of shrinkage-induced microcracking in the early age [70,71]. Unlike compressive strength, which is determined by the total porosity of the paste, the flexural strength obtained by three-point bending is very sensitive to the microcracking. As shown in section 3.5, AASF paste has a high potential of cracking due to restrained autogenous shrinkage. Although the paste samples for strength tests were not under externally restrained conditions during curing, the unreacted precursor particles, e.g. the spherical fly ash particles with crystalline phases, can locally restrain the shrinkage of gel surrounding them and thus induce microcracking [72]. The drying of the sample when exposed to the environment (RH of 50%) during strength test may induce additional shrinkage, although the exposure time of the samples before being tested was rather short (<30 min). When internal curing is applied to the paste, the

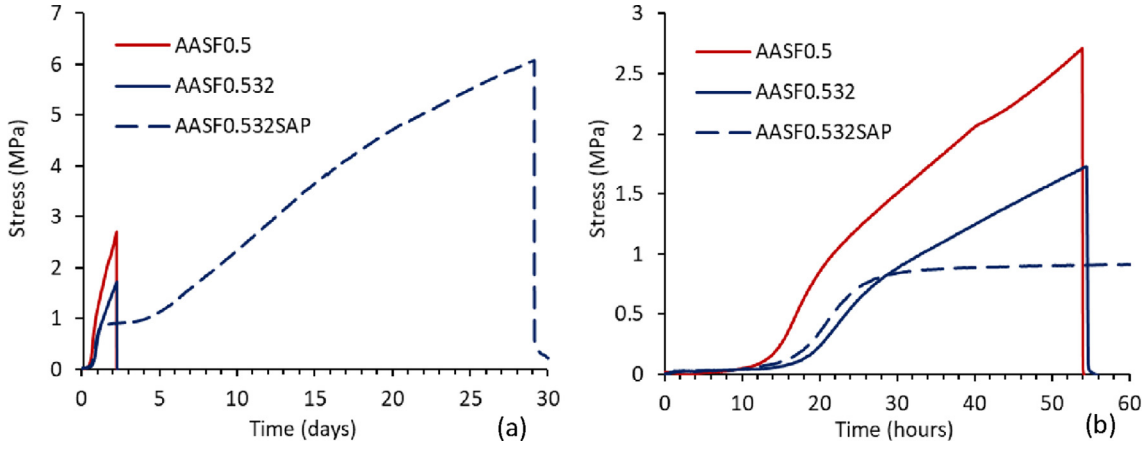

Fig. 11. Autogenous shrinkage-induced stress in AASF0.5, AASF0.552 and AASF0.552SAP (a), with the first 60 h amplified in (b).

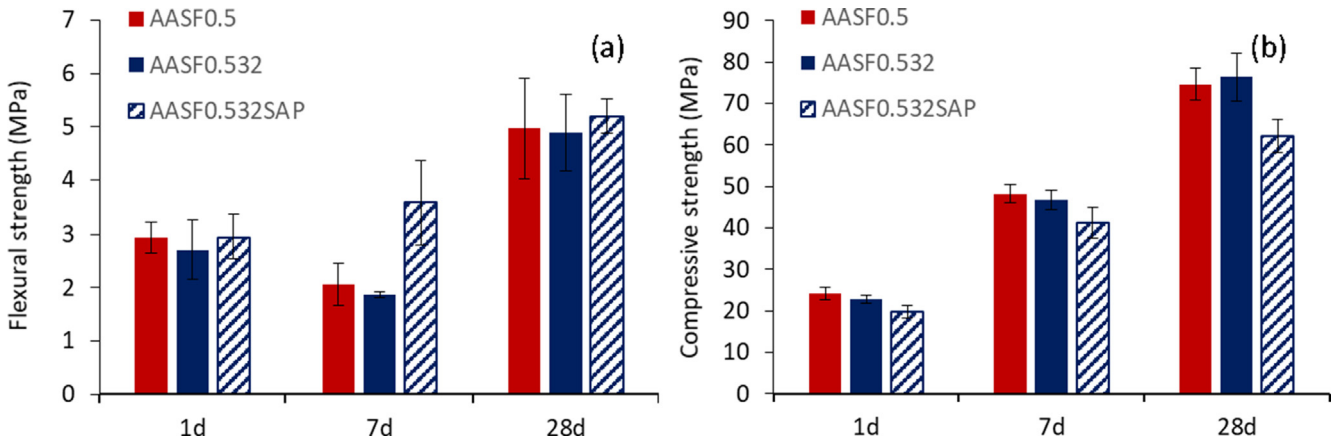

Fig. 12. Compressive (a) and flexural (b) strength of AASF pastes.

autogenous shrinkage and the cracking potential are greatly mitigated. The development of the microcracking due to early-age shrinkage would be effectively limited. Consequently, the flexural strength of AASF0.532SAP does not decrease with time and is much higher than those of the non-SAP pastes at 7 days. From 7 days to 28 days, the flexural strength of all mixtures increases due to the longer reaction time thus stronger structure. The incorporation of SAPs improves the flexural strength at all ages. The improved flexural strength is very important for a wider application of AASF, since this material is known to be more vulnerable to tensile failure than compressive failure [73–75].

The elastic modulus evolutions of AASF paste with and without SAP are shown in Fig. 13. It is interesting to observe that the elastic modulus of the pastes starts to develop rapidly only after the end of the dormant period, which is in the same pace as the development of internal stress (see Fig. 11). The increasing of the elastic modulus of AASF0.532SAP is slightly later than that of AASF0.5 (see the amplified area). This is in line with the slightly later appearance of the main reaction peak of AASF0.532 than AASF0.5, as shown in Fig. 5(a). The 7-days elastic modulus of AASF0.532SAP is slightly lower than that of AASF0.5. This seems consistent with the slightly lower reaction degree of the paste with SAP, as shown in Fig. 5(b).

The similar elastic modulus evolutions of AASF0.5 and AASF0.532SAP confirm that the greatly reduced stress in restrained AASF0.532SAP is not because of a reduced elastic modulus of the paste but because of the reduced autogenous shrinkage.

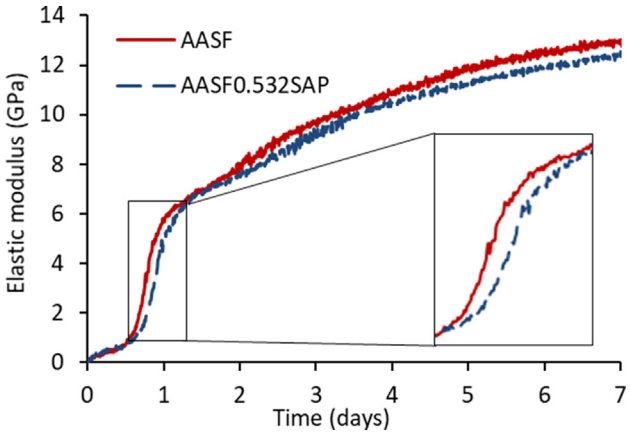

Fig. 13. Elastic modulus of AASF0.5 and AASF0.552SAP.

4. Conclusions

In this study, the effects of internal curing on the autogenous shrinkage, self-induced cracking and mechanical properties of AASF pastes are investigated. The following conclusions are drawn from the results of this study:

1. Internal curing by SAPs does not significantly influence the reaction products of AASF paste. The setting times of AASF0.532SAP is similar to that of AASF0.5. Besides the void originated from SAPs, the paste with SAPs shows similar pore structure to the control mixture.
2. In AASF0.532SAP, the absorption of activator by SAPs reaches the maximum before the initial setting of the paste. Afterwards, the liquid is gradually released from SAPs to the surrounding paste. The internal curing provided by the SAPs maintain a high RH in the paste.
3. Internal curing with SAPs can effectively mitigate the autogenous shrinkage of AASF paste, especially after the acceleration period. As a result, the cracking potential of AASF paste under restrained condition is also greatly mitigated by internal curing.
4. While the compressive strength of AASF paste can be slightly decreased by internal curing, the flexural strength is largely increased due to the mitigating effect on the development of microcracking by internal curing.
5. The improved performance, such as the mitigated autogenous shrinkage, the reduced cracking potential, and the enhanced flexural tensile strength, indicate that internal curing by SAPs serves as a very promising strategy in AASF towards its enhanced engineering performance and wider application in construction practise.

CRediT authorship contribution statement

Zhenming Li: Conceptualization, Methodology, Investigation, Writing - original draft, Writing - review & editing. **Shizhe Zhang:** Investigation. **Xuhui Liang:** Investigation. **José Granja:** Methodology. **Miguel Azenha:** Methodology, Writing - review & editing. **Guang Ye:** Supervision, Writing - review & editing.

Declaration of Competing Interest

The authors declare that they have no known competing financial interests or personal relationships that could have appeared to influence the work reported in this paper.

Acknowledgment

Zhenming Li and Xuhui Liang would like to acknowledge the funding supported by the China Scholarship Council (CSC) under grant No. 201506120072 and No. 201806050051. This work is supported also by the grant from the Netherlands Organisation for Scientific Research (NWO).

José Granja and Miguel Azenha would like to acknowledge Portuguese Foundation for Science and Technology (FCT) to fund the Research Project IntegraCrete (PTDC/ECM-EST/1056/2014 - POCI-01-0145-FEDER-016841). The grant UID/ECI/04029/2019 - ISISE, funded by national funds through the FCT/MCTES (PIDDAC) is also acknowledged.

Mateusz Wyrzykowski and Pietro Lura from Empa are gratefully acknowledged for supplying the SAPs and for the valuable discussions on the effect of the SAP.

References

[1] E. Worrell, L. Price, N. Martin, C. Hendriks, L.O. Meida, Carbon dioxide emissions from the global cement industry, Annu. Rev. Energy Environ. 26 (2001) 303–329.
[2] K.L. Scrivener, R.J. Kirkpatrick, Innovation in use and research on cementitious material, Cem. Concr. Res. 38 (2) (2008) 128–136.
[3] P. Peduzzi, Sand, rarer than one thinks, Environ. Dev. 11 (2014) 208–218.
[4] R.M. Andrew, Global CO_2 emissions from cement production, 1928–2017, Earth Syst. Sci. Data 10 (2018) 2213–2239, https://doi.org/10.5194/essd-10-2213-2018.
[5] C. Shi, A.F. Jiménez, A. Palomo, New cements for the 21st century: the pursuit of an alternative to Portland cement, Cem. Concr. Res. 41 (7) (2011) 750–763.
[6] J.L. Provis, J.S.J. Van Deventer, Alkali Activated Materials (2014), https://doi.org/10.1007/978-94-007-7672-2.
[7] J.L. Provis, S.A. Bernal, Geopolymers and related alkali-activated materials, Annu. Rev. Mater. Res. 44 (1) (2014) 299–327.
[8] B.C. McLellan, R.P. Williams, J. Lay, A. van Riessen, G.D. Corder, Costs and carbon emissions for geopolymer pastes in comparison to ordinary portland cement, J. Cleaner Prod. 19 (9-10) (2011) 1080–1090.
[9] G. Habert, C. Ouellet-Plamondon, Recent update on the environmental impact of geopolymers, RILEM Tech. Lett. 1 (2016) 17–23.
[10] M. Schneider, M. Romer, M. Tschudin, H. Bolio, Sustainable cement production—present and future, Cem. Concr. Res. 41 (7) (2011) 642–650.
[11] J.L. Provis, Geopolymers and other alkali activated materials: why, how, and what?, Mater. Struct. 47 (1-2) (2014) 11–25.
[12] M. Fawer, M. Concannon, W. Rieber, Life cycle inventories for the production of sodium silicates, Int. J. LCA 4 (4) (1999), https://doi.org/10.1007/BF02979498.
[13] O.M. Jensen, P.F. Hansen, Autogenous deformation and RH-change in perspective, Cem. Concr. Res. 31 (12) (2001) 1859–1865.
[14] Z. Li, J. Liu, G. Ye, Drying shrinkage of alkali-activated slag and fly ash concrete; A comparative study with ordinary Portland cement concrete, Heron 64 (2019) 149.
[15] N.K. Lee, J.G. Jang, H.K. Lee, Shrinkage characteristics of alkali-activated fly ash/slag paste and mortar at early ages, Cem. Concr. Compos. 53 (2014) 239–248.
[16] Z. Li, M. Nedeljkovic, Y. Zuo, G. Ye, Autogenous shrinkage of alkali-activated slag-fly ash pastes, in: 5th Int. Slag Valoris. Symp., Leuven, 2017, pp. 369–372.
[17] A.A. Melo Neto, M.A. Cincotto, W. Repette, Drying and autogenous shrinkage of pastes and mortars with activated slag cement, Cem. Concr. Res. 38 (4) (2008) 565–574.
[18] H. Ye, A. Radlińska, Shrinkage mechanisms of alkali-activated slag, Cem. Concr. Res. 88 (2016) 126–135.
[19] C. Li, H. Shi, W. Zhou, J. Cha, J. Huang, W. Shen, Influence of the thermal treatment process of MgO on alkali-activated cement, Bull. Chin. Ceram. Soc. 35 (2016) 632–637.
[20] Y. Yang, Z. Li, X. Zhang, J. Wei, Q. Yu, Reaction Mechanism of Compensating Shrinkage of Inorganic Polymer Pastes by Using Reactive MgO, J. South China Univ. Technol. (Natural Sci. Ed. 45 (2017) 102–109 (In Chinese).
[21] X. Hu, C. Shi, Z. Zhang, Z. Hu, Autogenous and drying shrinkage of alkali-activated slag mortars, J. Am. Ceram. Soc. 102 (8) (2019) 4963–4975.
[22] M. Palacios, F. Puertas, Effect of shrinkage-reducing admixtures on the properties of alkali-activated slag mortars and pastes, Cem. Concr. Res. 37 (5) (2007) 691–702.
[23] L. Kalina, E.B. Ková, J. Krouská, V.B. Jr., Polypropylene glycols as effective shrinkage-reducing admixtures in alkali-activated materials, Mater. J. 115 (n. d.). doi:10.14359/51701099
[24] M. Criado, A. Palomo, A. Fernández-Jiménez, P.F.G. Banfill, Alkali activated fly ash: effect of admixtures on paste rheology, Rheol. Acta 48 (4) (2009) 447–455.
[25] G. Habert, J.B. d'Espinose de Lacaillerie, N. Roussel, An environmental evaluation of geopolymer based concrete production: reviewing current research trends, J. Cleaner Prod. 19 (11) (2011) 1229–1238.
[26] C.A. Rees, J.L. Provis, G.C. Lukey, J.S.J. van Deventer, The mechanism of geopolymer gel formation investigated through seeded nucleation, Colloids Surf., A 318 (1-3) (2008) 97–105.
[27] V. Bilek Jr, L. Kalina, O. Fojtík, Shrinkage-Reducing Admixture Efficiency in Alkali-Activated Slag across the Different Doses of Activator, in: Key Eng. Mater., Trans Tech Publ, 2018, pp. 19–22.
[28] F. Collins, J.G. Sanjayan, Cracking tendency of alkali-activated slag concrete subjected to restrained shrinkage, Cem. Concr. Res. 30 (5) (2000) 791–798.
[29] Z. Li, M. Nedeljković, B. Chen, G. Ye, Mitigating the autogenous shrinkage of alkali-activated slag by metakaolin, Cem. Concr. Res. 122 (2019) 30–41.
[30] T. Bakharev, J.G. Sanjayan, Y.-B. Cheng, Effect of elevated temperature curing on properties of alkali-activated slag concrete, Cem. Concr. Res. 29 (10) (1999) 1619–1625.
[31] H. Ye, A. Radlińska, Shrinkage mitigation strategies in alkali-activated slag, Cem. Concr. Res. 101 (2017) 131–143.
[32] Z. Li, T. Lu, X. Liang, H. Dong, J. Granja, M. Azenha, G. Ye, Mechanisms of autogenous shrinkage of alkali-activated slag and fly ash pastes, Cem. Concr. Res. 135 (2020) 106107, https://doi.org/10.1016/j.cemconres.2020.106107.
[33] J.J. Thomas, A.J. Allen, H.M. Jennings, Density and water content of nanoscale solid C–S–H formed in alkali-activated slag (AAS) paste and implications for chemical shrinkage, Cem. Concr. Res. 42 (2) (2012) 377–383.
[34] M.R. Geiker, D.P. Bentz, O.M. Jensen, Mitigating autogenous shrinkage by internal curing, ACI Spec. Publ. (2004) 143–154.
[35] O.M. Jensen, P.F. Hansen, Water-entrained cement-based materials, Cem. Concr. Res. 31 (4) (2001) 647–654.
[36] G.R. de Sensale, A.F. Goncalves, Effects of fine LWA and SAP as internal water curing agents, Int. J. Concr. Struct. Mater. 8 (3) (2014) 229–238.
[37] O.M. Jensen, P. Lura, Techniques and materials for internal water curing of concrete, Mater. Struct. 39 (9) (2006) 817–825.
[38] V. Mechtcherine, M. Gorges, C. Schroefl, A. Assmann, W. Brameshuber, A.B. Ribeiro, D. Cusson, J. Custódio, E.F. da Silva, K. Ichimiya, S.-I. Igarashi, A. Klemm, K. Kovler, A.N. de Mendonça Lopes, P. Lura, V.T. Nguyen, H.-W. Reinhardt, R.D.T. Filho, J. Weiss, M. Wyrzykowski, G. Ye, S. Zhutovsky, Effect of internal curing by using superabsorbent polymers (SAP) on autogenous shrinkage and other properties of a high-performance fine-grained concrete: results of a RILEM round-robin test, Mater. Struct. 47 (3) (2014) 541–562.
[39] P. Lura, F. Durand, O.M. Jensen, Autogenous strain of cement pastes with superabsorbent polymers, Proc. Internaltional RILEM Conf. Vol. Chang. Hardening Concr. Test. Mitig. C (2006) 57–66. doi:10.1617/2351580052.007.
[40] J. Justs, M. Wyrzykowski, D. Bajare, P. Lura, Internal curing by superabsorbent polymers in ultra-high performance concrete, Cem. Concr. Res. 76 (2015) 82–90.
[41] D. Snoeck, O.M. Jensen, N. De Belie, The influence of superabsorbent polymers on the autogenous shrinkage properties of cement pastes with supplementary cementitious materials, Cem. Concr. Res. 74 (2015) 59–67.
[42] M. Wyrzykowski, P. Lura, Reduction of autogenous shrinkage in OPC and BFSC pastes with internal curing, in: Proc. XIII Int. Conf. Durab. Build. Mater. Components, São Paulo, Brazil, 2014, pp. 2–5.
[43] W. Tu, Y.u. Zhu, G. Fang, X. Wang, M. Zhang, Internal curing of alkali-activated fly ash-slag pastes using superabsorbent polymer, Cem. Concr. Res. 116 (2019) 179–190.
[44] S. Oh, Y.C. Choi, Superabsorbent polymers as internal curing agents in alkali activated slag mortars, Constr. Build. Mater. 159 (2018) 1–8.
[45] C. Song, Y.C. Choi, S. Choi, Effect of internal curing by superabsorbent polymers – internal relative humidity and autogenous shrinkage of alkali-activated slag mortars, Constr. Build. Mater. 123 (2016) 198–206.
[46] Z. Li, M. Wyrzykowski, H. Dong, J. Granja, M. Azenha, P. Lura, G. Ye, Internal curing by superabsorbent polymers in alkali-activated slag, Cem. Concr. Res. 135 (2020) 106123, https://doi.org/10.1016/j.cemconres.2020.106123.
[47] M. Wyrzykowski, S.-I. Igarashi, P. Lura, V. Mechtcherine, Recommendation of RILEM TC 260-RSC: using superabsorbent polymers (SAP) to mitigate autogenous shrinkage, Mater. Struct. 51 (5) (2018), https://doi.org/10.1617/s11527-018-1241-9.
[48] ASTM C 1608, Standard test method for chemical shrinkage of hydraulic cement paste, (2007) 667–670.
[49] Z. Li, S. Zhang, Y. Zuo, W. Chen, G. Ye, Chemical deformation of metakaolin based geopolymer, Cem. Concr. Res. 120 (2019) 108–118.
[50] K. Scrivener, R. Snellings, B. Lothenbach, A Practical Guide to Microstructural Analysis of Cementitious Materials, CRC Press, 2016.
[51] ASTM C191-18a, Standard Test Methods for Time of Setting of Hydraulic Cement by Vicat Needle, (2019) 1–8. doi:10.1520/C0191-18A.2.
[52] E.P. Barrett, L.G. Joyner, P.P. Halenda, The determination of pore volume and area distributions in porous substances. I. Computations from nitrogen isotherms, J. Am. Chem. Soc. 73 (1) (1951) 373–380.
[53] O.M. Jensen, P.F. Hansen, Autogenous relative humidity change in silica fume-modified cement paste, Adv. Cem. Res. 7 (25) (1995) 33–38.
[54] H. Huang, G. Ye, Examining the "time-zero" of autogenous shrinkage in high/ultra-high performance cement pastes, Cem. Concr. Res. 97 (2017) 107–114.
[55] P. Lura, O.M. Jensen, K. van Breugel, Autogenous shrinkage in high-performance cement paste: An evaluation of basic mechanisms, Cem. Concr. Res. 33 (2) (2003) 223–232.
[56] ASTM C1968, Standard Test Method for Autogenous Strain of Cement Paste and Mortar, (2013) 1–8. doi:10.1520/C1698-09.2.
[57] M. Grzybowski, S.P. Shah, Shrinkage cracking of fiber reinforced concrete, Mater. J. 87 (1990) 138–148.

[58] K. Kovler, J. Sikuler, A. Bentur, Restrained shrinkage tests of fibre-reinforced concrete ring specimens: effect of core thermal expansion, Mater. Struct. 26 (1993) 231–237.
[59] J.L. Schlitter, A.H. Senter, D.P. Bentz, T. Nantung, W.J. Weiss, A dual concentric ring test for evaluating residual stress development due to restrained volume change, J. ASTM Int. 7 (2010) 1–13.
[60] NEN 196-1, Methods of Testing Cement–Part 1: Determination of Strength, 2005, Eur. Comm. Stand. (2005).
[61] Miguel Azenha, Rui Faria, Filipe Magalhães, Leonel Ramos, Álvaro Cunha, Measurement of the E-modulus of cement pastes and mortars since casting, using a vibration based technique, Mater. Struct. 45 (1-2) (2012) 81–92.
[62] W.K.W. Lee, J.S.J. van Deventer, Use of infrared spectroscopy to study geopolymerization of heterogeneous amorphous aluminosificates, Langmuir. 19 (2003) 8726–8734. doi:Doi 10.1021/La026127e
[63] I. García Lodeiro, A. Fernández-Jimenez, A. Palomo, D.E. Macphee, Effect on fresh C-S-H gels of the simultaneous addition of alkali and aluminium, Cem. Concr. Res. 40 (1) (2010) 27–32.
[64] Ines García-Lodeiro, A. Fernández-Jiménez, M. Teresa Blanco, Angel Palomo, FTIR study of the sol–gel synthesis of cementitious gels: C–S–H and N–A–S–H, J. Sol-Gel Sci. Technol. 45 (1) (2008) 63–72.
[65] M. Nedeljković, Carbonation mechanism of alkali-activated fly ash and slag materials: In view of long-term performance predictions, Delft University of Technology, 2019.
[66] I. Garcia-Lodeiro, A. Palomo, A. Fernández-Jiménez, D.E. Macphee, Compatibility studies between N-A-S-H and C-A-S-H gels. Study in the ternary diagram Na2O–CaO–Al2O3–SiO2–H2O, Cem. Concr. Res. 41 (9) (2011) 923–931.
[67] Janis Justs, Mateusz Wyrzykowski, Frank Winnefeld, Diana Bajare, Pietro Lura, Influence of superabsorbent polymers on hydration of cement pastes with low water-to-binder ratio: a calorimetry study, J. Therm. Anal. Calorim. 115 (1) (2014) 425–432.
[68] ASTM C 1581, Standard Test Method for Determining Age at Cracking and Induced Tensile Stress Characteristics of Mortar and Concrete under Restrained Shrinkage, ASTM Int. (2009) 1–7. doi:10.1520/C1581.
[69] British Standards Institution, Eurocode 2: Design of concrete structures: Part 1-1: General rules and rules for buildings, British Standards Institution, 2004.
[70] Frank Collins, J.G. Sanjayan, Microcracking and strength development of alkali activated slag concrete, Cem. Concr. Compos. 23 (4-5) (2001) 345–352.
[71] M. Nedeljković, Z. Li, G. Ye, Setting, Strength, and Autogenous Shrinkage of Alkali-Activated Fly Ash and Slag Pastes: Effect of Slag Content, Materials (Basel). 11 (2018) 2121. doi:10.3390/ma11112121
[72] Pietro Lura, Ole Mejlhede Jensen, Jason Weiss, Cracking in cement paste induced by autogenous shrinkage, Mater. Struct. 42 (8) (2009) 1089–1099.
[73] Zhenming Li, Shizhe Zhang, Xuhui Liang, Guang Ye, Cracking potential of alkali-activated slag and fly ash concrete subjected to restrained autogenous shrinkage, Cem. Concr. Compos. 114 (2020) 103767, https://doi.org/10.1016/j.cemconcomp.2020.103767.
[74] Cengiz Duran Atiş, Cahit Bilim, Özlem Çelik, Okan Karahan, Influence of activator on the strength and drying shrinkage of alkali-activated slag mortar, Constr. Build. Mater. 23 (1) (2009) 548–555.
[75] Guohao Fang, Wing Kei Ho, Wenlin Tu, Mingzhong Zhang, Workability and mechanical properties of alkali-activated fly ash-slag concrete cured at ambient temperature, Constr. Build. Mater. 172 (2018) 476–487.